

***Ab initio* phonon scattering by dislocations**Tao Wang,^{1,*} Jesús Carrete,² Ambroise van Roekeghem,³ Natalio Mingo,³ and Georg K. H. Madsen^{2,†}¹CMAT, ICAMS, Ruhr-Universität Bochum, 44780 Bochum, Germany²Institute of Materials Chemistry, TU Wien, A-1060 Vienna, Austria³LITEN, CEA-Grenoble, 38054 Grenoble Cedex 9, France

(Received 8 February 2017; published 6 June 2017)

Heat management in thermoelectric and power devices as well as in random access memories poses a grand challenge and can make the difference between a working and an abandoned device design. Despite the prevalence of dislocations in all these technologies, the modeling of their thermal resistance is based on 50-year-old analytical approximations, whose simplicity was driven by practical limitations rather than physical insight. We introduce an efficient *ab initio* approach based on Green's functions computed by two-dimensional reciprocal space integration. By combining elasticity theory and density functional theory, we calculate the scattering strength of a 90° misfit edge dislocation in Si. Because of the breakdown of the Born approximation, earlier literature models fail, even qualitatively. We find that a dislocation density larger than 10⁹ cm⁻² is necessary to substantially influence thermal conductivity at room temperature and above. We quantify how much of the reduction of thermal conductivity measured in nanograined samples can be explained by realistic dislocation concentrations.

DOI: 10.1103/PhysRevB.95.245304

I. INTRODUCTION

The length scales of modern semiconductor architectures have long passed below the intrinsic mean free paths of the heat-carrying phonons in the underlying materials [1], making predictive modeling of the thermal transport an inherently multiscale problem. Despite the prevalence of dislocations in all these technologies [2–4], the modeling of their contribution to thermal resistance is based on 50-year-old analytical approximations [5–7]. Due to the assumptions underlying their derivation, these models can differ by several orders of magnitude, both with respect to each other and with respect to experiment [7]. Phonon scattering by dislocations can be modeled at an atomic level by molecular dynamics simulations [8,9]. However, due to the length and time scales involved, these calculations have to rely on semiempirical potentials which inherently are limited when it comes to transferability and quantitative predictive power of thermal conductivity [10].

The multiscale nature of phonon transport leads to the basic dilemma of, on one hand, the need for a density functional theory (DFT) level of precision [11,12] and, on the other hand, the need for large length scales to quantify the phonon-scattering strength caused by various types of defects, e.g., vacancies, interfaces, and dislocations, inside the materials. For the quantification of defect scattering, the Green's-function approach [13–15] would seem ideal. It can rely on DFT for the calculation of the scattering matrix elements and be combined with the Boltzmann transport equation to describe anharmonic systems. When applied to interfaces [16] and point defects [17,18] good agreement with experiment has been found.

The lack of applications of the Green's-function approach can partly be attributed to the large model sizes needed to calculate converged numbers for, e.g., dislocation structures. In the present paper we combine elasticity theory with DFT to show how the quantitative predictive calculation of phonon

scattering can be extended to dislocations. We do this by calculating the energy- and momentum-dependent scattering rate of a quadrupolar arrangement of 90°-misfit dislocations in Si. The structures are set up using elasticity theory, whereby the dislocation structure can be controlled precisely. The scattering rates are obtained by dividing the three-dimensional Brillouin zone (BZ) into parallel planes perpendicular to the defect line. We find that the obtained scattering rates deviate, even qualitatively, from the simple historical approximations.

II. BACKGROUND**A. Supercell approach**

The calculations are performed using a supercell approach. The supercell is built from four-atom unit cells, each containing a bilayer along the dislocation direction (Fig. 1). The dislocation line direction \mathbf{a}_1 is parallel to [1̄10] in the original cubic diamond unit cell, Fig. 1. \mathbf{a}_2 is parallel to the Burgers vector \mathbf{b} and the [110] direction of the cubic cell. The final direction $\mathbf{a}_3 \parallel [112]$ is determined by the quadrupolar ordering of the dislocation cores [19,20]. The intuitively simplest way to introduce an edge dislocation into the crystal structure of silicon is by a cut and shift procedure according to the corresponding geometrical definition. However, such a starting configuration necessitates a large geometrical reconstruction during atomic relaxation [19]. Instead, the dislocations are introduced into the initial structure by mapping the elastic deformation field due to the array of edge dislocations to the atoms in the supercell (Fig. 1). In elasticity theory [21], the deformed materials have to fulfill the force balance equation, which, for the current case, leads to a fourth-order harmonic partial differential equation. The differential equation under the specific boundary conditions for an edge dislocation,

$$\mathbf{u} = \begin{cases} 0, & \theta = 0, \\ \mathbf{b}, & \theta = 2\pi \end{cases} \quad (1)$$

can be solved to obtain the displacement field around the dislocation core (details in the Supplemental Material [22]).

*tao.wang@rub.de

†georg.madsen@tuwien.ac.at

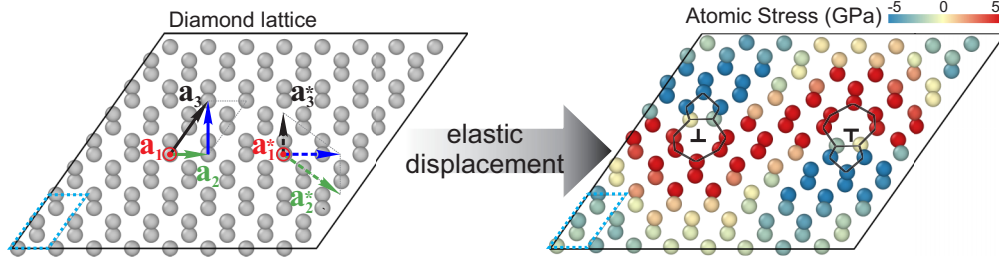


FIG. 1. The supercell used to set up a quadrupolar arrangement of $\mathbf{b} = (a/2)\langle 110 \rangle$ edge dislocations, where \mathbf{b} is the Burgers vector, a is the lattice constant of the conventional cubic cell, and $\langle 110 \rangle$ is the equivalent directions. In the left pane the blue cell illustrates the four-atom cell used to set up the 8×4 supercell. The vectors give the directions of the supercell axes in the conventional diamond-lattice cell. The right panel shows the structure after mapping the elastic displacement field and DFT relaxation. The dislocation cores are marked by \perp , and the seven- and fivefold rings are shown by atoms connected by black lines. The atoms are colored according to the σ_{22} component of the virial stress tensor with red corresponding to a tensile and blue corresponding to a compressive strain.

Using this procedure we obtain a starting structure close to the optimal one, thereby greatly reducing the number of computational steps required for the geometry optimization.

B. Green's function approach

The scattering of phonons due to defects is predominantly elastic and can be expressed using the **T**-matrix formalism [17,23,24]. In the present paper we extend the earlier formalism to a one-dimensional periodic defect where a conserved wave number can be defined. In the setup illustrated in Fig. 1 the periodicity is along \mathbf{a}_1 , which is parallel to \mathbf{a}_1^* . We can thus introduce a mixed-space basis of states with well-defined values of q_1 ,

$$|\phi(q_1)\rangle = \sum_l e^{iq_1 R_l} |\phi(l)\rangle. \quad (2)$$

Consequently, the perturbation cannot mix states with different values of q_1 . The **T**-matrix $\mathbf{T} = \mathbf{V} + \mathbf{VgT}$ is then expressed as

$$\mathbf{T}^+(q_1, \omega^2) = [\mathbf{I} - \mathbf{V}(q_1)\mathbf{g}^+(q_1, \omega^2)]^{-1}\mathbf{V}(q_1). \quad (3)$$

The scattering rate on the q_1 Brillouin-zone plane can then be expressed as

$$\tau_{\lambda, q_1}^{-1} = \frac{S}{\omega_{\lambda, q_1}} \sum_{\lambda', q'_1} |\langle \phi_{\lambda'}(q'_1) | \mathbf{T}^+(q_1, \omega^2) | \phi_{\lambda}(q_1) \rangle|^2 \delta(\omega'^2 - \omega^2), \quad (4)$$

where ϕ is the phonon state indexed by q_1 and the compound index λ of q_2, q_3 , and the index of the phonon state ($1 \leq j \leq 12$ in the four-atom primitive cell, see Fig. 1). $\omega_{\lambda}(q_1)$ is the dispersion on the plane. $|\phi_{\lambda'}(q'_1)\rangle$ and $|\phi_{\lambda}(q_1)\rangle$ are the corresponding final and incident eigenstates, respectively. S is the ratio of the normalization area of the eigenvector and the scatterer's area. Equation (4) gives the contribution of each final eigenstate to the total scattering strength. By employing the optical theorem, the scattering rate can be rewritten as

$$\tau_{\lambda, q_1}^{-1} = -\frac{S}{\omega_{\lambda, q_1}} \text{Im}\{\langle \phi_{\lambda}(q_1) | \mathbf{T}^+(q_1, \omega^2) | \phi_{\lambda}(q_1) \rangle\}. \quad (5)$$

The two expressions must give the same results, but Eq. (5) is more efficient to evaluate numerically than Eq. (4). The **T** matrix can also be approximated according to the Born

approximation by truncating the Born series for the perturbed states,

$$|\psi\rangle = |\phi\rangle + \mathbf{g}(\omega^2)\mathbf{V}|\phi\rangle + [\mathbf{g}(\omega^2)\mathbf{V}]^2|\phi\rangle + \dots, \quad (6)$$

at first order.

III. COMPUTATIONAL PROCEDURE

The DFT calculations were carried out using VASP [25,26] with the local density approximation. The force calculations are performed using the projector-augmented-wave method (with a cutoff of 430 eV) and a $4 \times 2 \times 2$ k -point mesh. The second-order interatomic force constants (IFCs) are built using the PHONOPY package [27]. The third-order IFCs of the unperturbed cell are calculated by systematically displacing the atoms pairwise and collecting the resulting DFT force [28]. The phonon band structures of the dislocation structure also were checked. No negative frequencies were observed, showing that the supercell is stable. The mass-disorder scattering due to isotopes was evaluated according to Ref. [29].

To obtain the perturbation matrix V we treat each dislocation pair as an independent scattering center. V then is calculated by displacing each atom in the defected supercell, Fig. 1, individually and obtaining the forces. A fully relaxed supercell with the size of $3 \times 8 \times 4$ times the specific four-atom unit cell, containing 384 atoms in total, was used for the force constant calculations (details of the convergence tests can be found in the Supplemental Material [22]). As the dislocations break the cubic symmetry this corresponds to a large number of displacements, and this step is computationally the most costly. Further details for the calculation of the IFCs that are necessary to obtain the perturbation matrix and Green's function are documented in the Supplemental Material [22].

To obtain \mathbf{g} the three-dimensional (3D) BZ is divided into parallel planes spanned by $\mathbf{a}_2^* - \mathbf{a}_3^*$. A triangulation scheme followed by barycentric interpolation in the triangles as described in the Appendix is adopted to discretize each of the two-dimensional BZ planes. This treatment allows us to split the three-dimensional domain into independent two-dimensional domains.

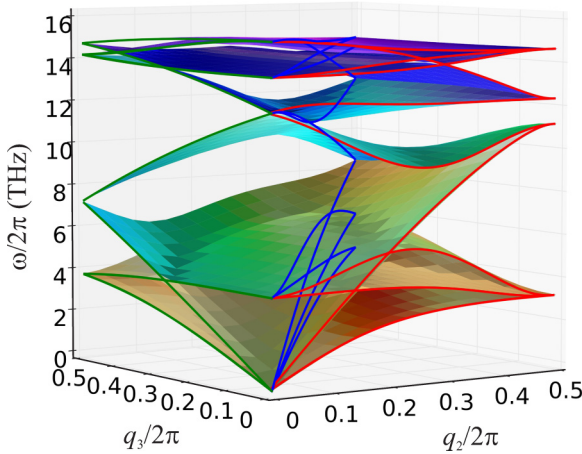


FIG. 2. Phonon band structure of silicon on the $q_1 = 0$ plane of the Brillouin zone of the four-atom unit cell shown in Fig. 1. The three directions are on the $q_1 = 0$ plane and are parallel to the Burgers vector $\mathbf{q}_{\parallel} \parallel \mathbf{a}_2^* + \mathbf{a}_3^*$ (blue), perpendicular to the Burgers vector $\mathbf{q}_{\perp} \parallel \mathbf{a}_3^*$ (green) and the intermediate direction $\mathbf{q}_{\angle} \parallel \mathbf{a}_2^*$ (red), Fig. 1.

IV. RESULTS AND DISCUSSION

The optimized edge dislocation structure is shown in Fig. 1. Known edge dislocation core structures composed of a five-atom- and a seven-atom-ring pattern [20] can be observed, thereby underlining the reliability of the approach. Except for the atoms making up the dislocation core, all atoms possess a strained cubic diamond crystal structure.

The phonon band structure of the defect-free Si is shown in Fig. 2. The dispersion along the three selected directions \mathbf{q}_{\parallel} , \mathbf{q}_{\perp} , and \mathbf{q}_{\angle} is marked. One potential shortcoming of the analytic approximations of dislocation scattering [5–7] is that they are limited to the Born approximation, obtained by truncating the Born series for the perturbed states at the first order, instead of the full T-matrix formalism Eqs. (3)–(5). Based on the IFCs obtained with DFT, the scattering rates are calculated using both the Born approximation and the T-matrix formalism, Fig. 3. Using the Born approximation we recover a monotonically increasing scattering rate for phonons with

frequencies up to 1 THz, similar to early analytic results [5–7]. However, at higher frequencies, corresponding to wave vectors away from the center of the BZ, the scattering deviates from a monotonic behavior. Furthermore, the τ^{-1} 's computed based on the T-matrix method deviate strongly from those obtained with the Born approximation, Fig. 3. This is understandable as the dislocations strongly perturb the environment of the neighboring atoms and underline that the assumptions behind the analytic results compromise their precision. Interestingly, in the Born approximation the trend for the low-frequency phonons is closer to a ω^3 behavior, which would be expected for a line of point defects, indicating that the dislocation core structure is important in determining the scattering [6,7]. However, we underline that this trend only covers a very small part of the BZ, which is mainly noticeable due to the log-log scale used in Fig. 3, meaning that it will only substantially contribute to lowering the thermal conductivity at very low temperatures.

The anisotropy in the dependence of the scattering rate on the direction of the \mathbf{q} vector, that can clearly be seen in Fig. 3, can originate from the heterogeneous strain field. An analytic model based on a theoretical study of an edge dislocation embedded in an infinite homogeneous elastic medium [7]

predicted a ratio of $\tau_{\parallel b}^{-1}/\tau_{\perp b}^{-1} = 2/[1 + (\frac{v}{1-v})^2]$, where v is Poisson's ratio. However, Fig. 3 shows that the constant ratio between $\tau_{\parallel b}^{-1}$ and $\tau_{\perp b}^{-1}$ can only be reproduced for one of the branches due to the strongly perturbed atomic environment by the dislocation cores. Furthermore, for Si, Poisson's ratio is $v \approx 0.28 (< 1/2)$, and the analytic models would thus lead to a prediction of $\tau_{\parallel b}^{-1} > \tau_{\perp b}^{-1}$. Figure 3 on the other hand shows that $\tau_{\perp b}^{-1}$ can be even larger than $\tau_{\parallel b}^{-1}$, indicating the failure of a model based purely on the strain field and the Born approximation.

Figure 4 shows the dislocation scattering in comparison to the phonon-phonon and isotope scatterings for the entire BZ. The $\tau_{qj}^{-1}|_{\text{disloc}}$'s are calculated according to Eqs. (3)–(5). The three-phonon scattering rates are obtained on the same transport \mathbf{q} mesh according to the procedure explained earlier [28]. It is apparent that the increasing trend only is found in a small part of the BZ and for certain directions in

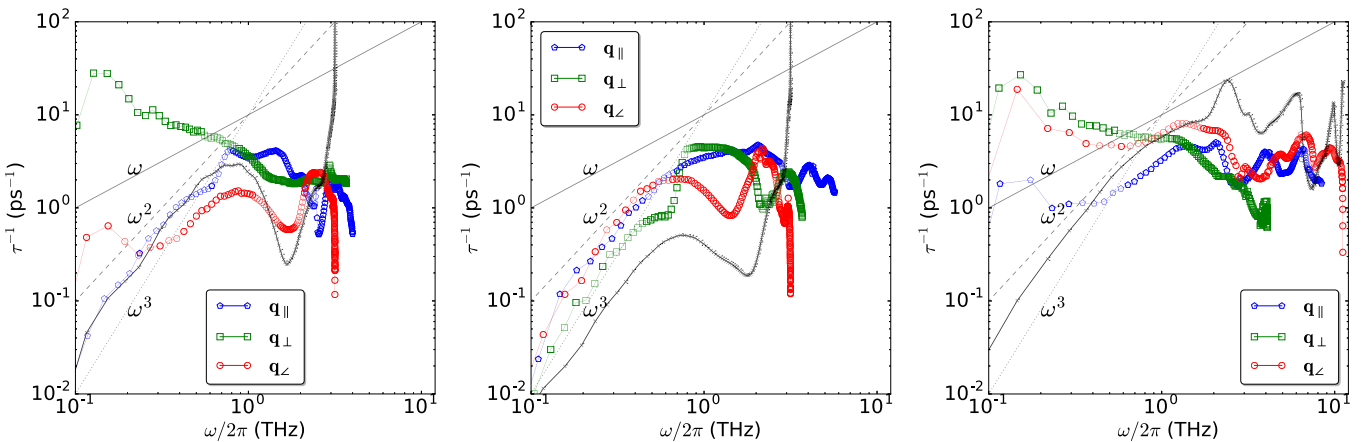


FIG. 3. The scattering rate for the three acoustic phonon branches along three selected directions of \mathbf{q} . The directions are labeled as explained in Fig. 2 and are calculated using the T matrix. The black dots correspond to the scattering rates obtained with the Born approximation along \mathbf{q}_{\angle} .

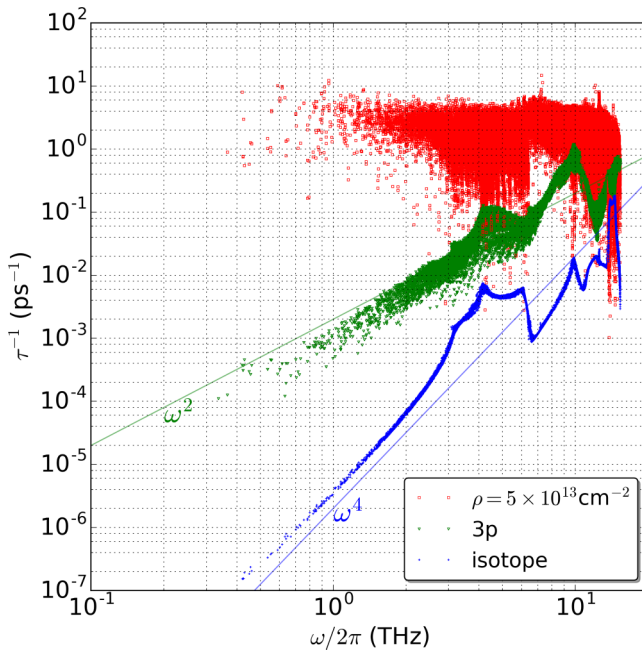


FIG. 4. Different scattering rates computed in the current calculation: three-phonon scattering, phonon-dislocation scattering, and isotope scattering. The three-phonon scattering was calculated at 300 K. The dislocation scattering is computed from the \mathbf{T} matrix and the Green's functions Eqs. (3)–(5). The points correspond to a $34 \times 34 \times 28$ q mesh. For clarity, the scattering rates have been calculated for a very high dislocation density ($\rho = 5 \times 10^{13} \text{ cm}^{-2}$). Changing the dislocation density to, e.g., $\rho = 10^{11} \text{ cm}^{-2}$ would rigidly shift the red points by the same magnitude, i.e., from being centered around $\tau^{-1} = 5$ to around $\tau^{-1} = 10^{-2} \text{ ps}^{-1}$.

agreement with the earlier observations. The overall behavior is better understood as a ω^0 behavior, similar to the usual models of grain boundaries. This makes sense taking into account that the structure of small-angle grain boundaries can be understood as a lineup of edge dislocations [30]. However, it is also clear that a constant ω^0 behavior is a very approximate description and that the actual dislocation scattering rates vary by two to three orders of magnitude. It clearly is seen that, even for a dislocation density that is two to three orders of magnitude smaller than that used to make Fig. 4, corresponding to a realistic [31,32] dislocation density of $\rho \approx 10^{10}\text{--}10^{11} \text{ cm}^{-2}$, the scattering due to dislocations is comparable to the phonon-phonon scattering at room temperature.

Within the relaxation time approximation the thermal conductivity tensor can be estimated by summing all the excited phonons in the BZ as

$$\kappa_t = \sum_j \int_{\text{BZ}} C_{\mathbf{q},j} \mathbf{v}_{\mathbf{q},j} \otimes \mathbf{v}_{\mathbf{q},j} \tau_{\mathbf{q},j} \frac{d\mathbf{q}}{8\pi^3}, \quad (7)$$

where $\mathbf{v}_{\mathbf{q},j}$, $\tau_{\mathbf{q},j}$, and $C_{\mathbf{q},j}$ are the group velocity and lifetime of the j th branch phonon with wave-number \mathbf{q} and its contribution to the heat capacity. Based on Matthiessen's rule, the total scattering strength $\tau_{\mathbf{q},j}^{-1}$ for each phonon \mathbf{q},j can be summed together over all the possible scattering processes in

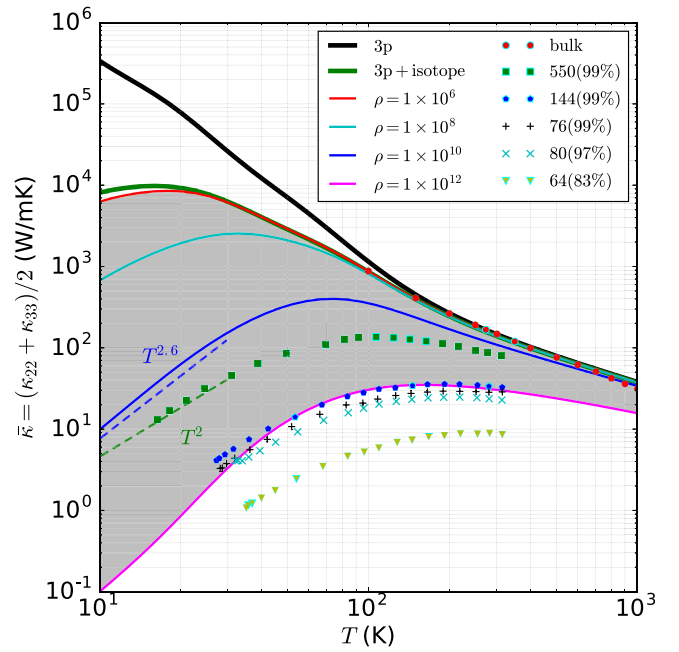


FIG. 5. Temperature-dependent thermal conductivity of silicon computed with various scattering mechanisms. The gray area stands for the influence region of dislocation with the line density range from $\rho = 10^6$ to $\rho = 10^{12} \text{ cm}^{-2}$. The experimental data are taken from Ref. [31] and labeled with their average grain size in nanometers and density in percentages of pure Si as in the original work.

the material,

$$\tau_{\mathbf{q},j}^{-1} = \tau_{\mathbf{q},j}^{-1}|^{(3p)} + \tau_{\mathbf{q},j}^{-1}|^{(\text{isotope})} + \tau_{\mathbf{q},j}^{-1}|^{(\text{disloc})} + \dots \quad (8)$$

With the computed scattering rates, Fig. 4 as well as phonon dispersion, Fig. 2, the thermal conductivity is ready for evaluation according to Eq. (7). The scattering rates and velocities are computed on the same transport $34 \times 34 \times 28$ q mesh. The nonequal numbers of the q points along the three reciprocal axes are necessary due to the nonequal lengths of the reciprocal lattice vectors of our specific four-atom unit cell, Fig. 1. For the Green's-function calculations a much denser $34 \times 80 \times 80$ q mesh was used (see the Supplemental Material for the grid mesh convergence check [22]).

Figure 5 shows the temperature dependence of the thermal conductivity of silicon when various dislocation densities are considered. When the thermal conductivity of bulk silicon is computed by considering only anharmonic and isotope phonon scatterings we obtain a $\kappa = 139 \text{ W/mK}$ at 300 K. The value agrees well with experimental data for bulk silicon with an underestimation of about 10% due to the use of the relaxation time approximation [11,12]. Phonon-dislocation scattering is averaged over all directions on the plane to simulate a random orientation of the dislocations and the overall thermal conductivity as shown in Fig. 5. With the increase in temperature, the anharmonic scattering tends to dominate the total scattering strength, which means that dislocation densities ρ larger than 10^9 cm^{-2} are necessary to substantially influence the thermal transport. However, in agreement with the discussion of Fig. 4 it is clearly seen that, for a realistic dislocation density around $\rho \approx 10^{10}\text{--}10^{11} \text{ cm}^{-2}$,

the scattering due to dislocations plays a substantial role in lowering the thermal conductivity.

The experimental data in Fig. 5 are taken from a systematic study of lattice thermal conductivity of nanograined Si as a function of average grain size by Wang *et al.* [31]. Wang *et al.* showed that low-temperature dependence of κ followed a T^2 trend and interpreted this in terms of a grain-size distribution. A different interpretation was proposed by Kim *et al.* [33] who modeled the data based on a ω^1 and ω^3 dependence of dislocation scattering. A fair conclusion of these two studies probably is that the experimental data can be fitted by a combination of a Debye model with a power-law description of the scattering. However, to explain the experimental data and discriminate between scattering mechanisms, a quantitative predictive methodology is necessary. Figure 5 illustrates how dislocation scattering can indeed go a long way to explain the magnitude of the experimental lowering of thermal conductivity due to grain-size reduction. Dislocation scattering furthermore lowers the T^3 -bulk trend to a $T^{2.6}$ -bulk trend but is not enough to reproduce the T^2 trend. We interpret this as indicating that further scattering mechanisms, such as grain-size distribution [31,34] play an important role in the experimental data.

V. CONCLUSION

We have introduced a Green's-function-based method to quantitatively predict the phonon-scattering strength of dislocations at the precision of density functional theory. A systematic approach based on elasticity theory was used to set up the atomic model. The mapping of the elastic strain field to atomic displacements can be extended to complex dislocation array structures via well-developed discrete dislocation dynamics modeling approaches [35]. It was found that a dislocation density larger than $\rho = 10^9 \text{ cm}^{-2}$ is necessary to substantially influence thermal conductivity at room temperature and above. Interestingly, this is the dislocation density range found in the buffer layers of GaN-based devices, which have been suggested to play an important role in thermal resistance [36].

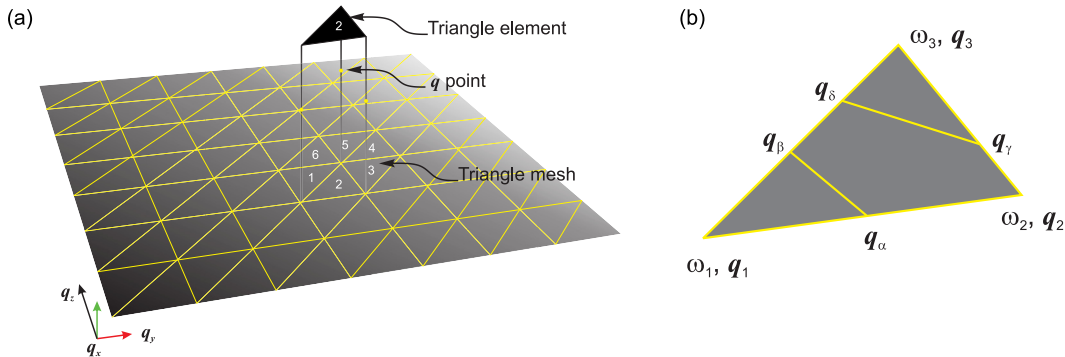


FIG. 6. (a) Two-dimensional q_x plane discretized in triangular elements used to compute the Green's function. (b) Interpolation over the one-triangle element. The vertices are labeled so that $\omega_1^2 \leq \omega_2^2 \leq \omega_3^2$. When $\omega_1^2 < \omega^2 \leq \omega_2^2$, only the subtriangle with vertices $(\mathbf{q}_1, \mathbf{q}_\alpha, \mathbf{q}_\beta)$ contributes to the imaginary part where the interpolated dispersions are $\mathbf{q}_\alpha = E_{12}\mathbf{q}_1 + E_{21}\mathbf{q}_2$ and $\mathbf{q}_\beta = E_{13}\mathbf{q}_1 + E_{31}\mathbf{q}_3$. When $\omega_2^2 < \omega^2 \leq \omega_3^2$, only the tetragon with vertices $(\mathbf{q}_1, \mathbf{q}_2, \mathbf{q}_\gamma, \mathbf{q}_\delta)$ contributes with interpolated $\mathbf{q}_\gamma = E_{23}\mathbf{q}_2 + E_{32}\mathbf{q}_3$ and $\mathbf{q}_\delta = E_{13}\mathbf{q}_1 + E_{31}\mathbf{q}_3$.

ACKNOWLEDGMENTS

C. Begau is thanked for helpful discussions concerning elasticity theory. We acknowledge support from EU Horizon 2020 Grant No. 645776 (ALMA).

APPENDIX: TWO-DIMENSIONAL GREEN'S FUNCTION TRIANGULATION SCHEME

Based on the precomputed IFCs for the defect-free system, the dispersion relation $\omega(\mathbf{q})$ in the given \mathbf{q} mesh of the BZ can be obtained. Together with ω_{λ, q_1} , the integral form of the Green's function on each plane can be computed as

$$g_{i,j}^+(\omega^2, q_1) = \sum_{\lambda} \langle \phi_{\lambda}(q_1) | i \rangle \langle j | \phi_{\lambda}(q_1) \rangle W_{\lambda}(\omega^2; q_1), \quad (\text{A1})$$

where the weight function $W_{\lambda}(\omega^2; q_1)$ is obtained via a two-dimensional integral of the spectral function for each branch and q_1 . In order to evaluate W accurately each dispersion surface ω_{λ}^2 is sampled using a regular grid. The grid is triangulated, and each dispersion is approximated by linear interpolation in barycentric coordinates inside each of the triangles. Under these approximations, analytic expressions can be derived for the real and imaginary contributions to W from each triangle and the total weight is a sum of these contributions,

$$W(\omega^2; q_1) = \sum_n \sum_i w_i^n(\omega^2; q_1), \quad (\text{A2})$$

where n indexes the triangles, i indexes the vertices, and the branch indices have been suppressed.

The triangulation scheme is adapted from the earlier work [37,38]. The equations for the real part as listed in Ref. [38] contain errors and are corrected here. Only the final equations are listed here, whereas the detailed derivation procedure can be found in Refs. [37,38]. Taking the one-triangle element with vertices \mathbf{q}_{1-3} each with the associated frequencies ω_{1-3}^2 , Fig. 6(b), we first define E_{ij} ,

$$E_{ij} = \frac{\omega^2 - \omega_i^2}{\omega_j^2 - \omega_i^2}. \quad (\text{A3})$$

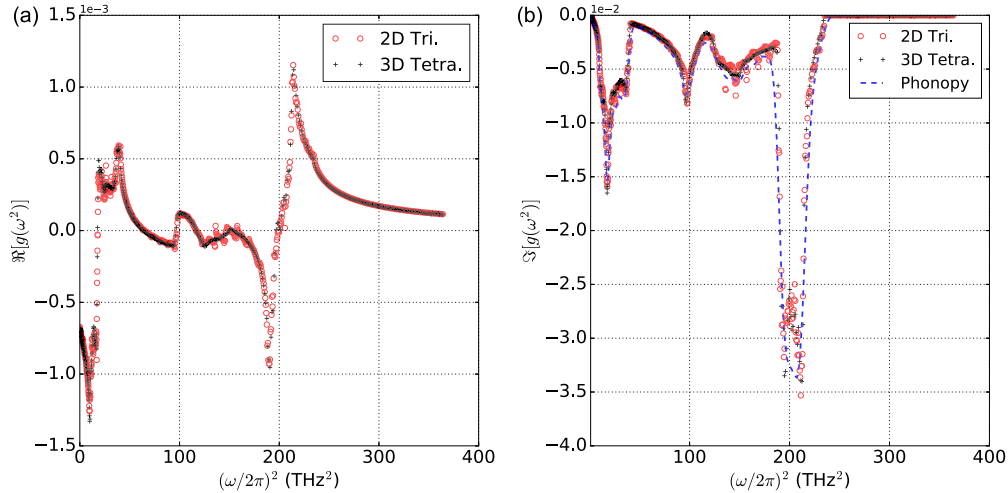


FIG. 7. (a) Real part and (b) imaginary part of $g(\omega^2)$ contributed by summing all the planes. The black crosses on the curves stand for the results obtained using the tetrahedron method [39] implemented in the ALMABTE code [40]. The blue curve is the density of states obtained from PHONOPY. The IFCs are obtained using DFT.

Let $D_1 = E_{21}E_{31}$, $D_3 = E_{13}E_{23}$, $X_i = \omega^2 - \omega_i^2$, and S_t be the area of the triangle. When $\omega^2 \in (\omega_1^2, \omega_2^2]$, only the subtriangle with vertices $(\mathbf{q}_1, \mathbf{q}_\alpha, \mathbf{q}_\beta)$, Fig. 6(b), contributes to the imaginary part,

$$\text{Im}[w_i(\omega^2)] = \begin{cases} \frac{E_{12}+E_{13}}{\omega^2-\omega_1^2} D_1 S_t, & i = 1, \\ \frac{E_{11}}{\omega^2-\omega_1^2} D_1 S_t, & i = 2,3. \end{cases} \quad (\text{A4})$$

The real part is obtained via an analytic Hilbert transform of the imaginary part,

$$\text{Re}[w_i(\omega^2)] = \begin{cases} \left[\frac{E_{21} \ln \left| \frac{X_1}{X_2} \right| (E_{12} + E_{13}) + \frac{1}{2}(E_{21} - E_{12}) - E_{13}}{\omega_1^2 - \omega_3^2} - \frac{\omega_2^2 - \omega_1^2}{2(\omega_1^2 - \omega_3^2)^2} \right] S_t, & i = 1, \\ \left[\frac{E_{21} \ln \left| \frac{X_1}{X_2} \right| E_{21} - E_{21}}{\omega_1^2 - \omega_3^2} - \frac{1}{2(\omega_1^2 - \omega_3^2)} \right] S_t, & i = 2, \\ \left[\frac{E_{21} \ln \left| \frac{X_1}{X_2} \right| E_{31} - E_{31}}{\omega_1^2 - \omega_3^2} - \frac{\omega_1^2 - \omega_2^2}{2(\omega_1^2 - \omega_3^2)^2} \right] S_t, & i = 3. \end{cases} \quad (\text{A5})$$

When $\omega^2 \in (\omega_2^2, \omega_3^2]$, only the triangle with vertices $(\mathbf{q}_1, \mathbf{q}_2, \mathbf{q}_\gamma, \mathbf{q}_\delta)$, Fig. 6(b), contributes

$$\text{Im}[w_i(\omega^2)] = \begin{cases} \frac{E_{i3}}{\omega_3^2 - \omega^2} D_3 S_t, & i = 1,2, \\ \frac{E_{31} + E_{32}}{\omega_3^2 - \omega^2} D_3 S_t, & i = 3, \end{cases} \quad (\text{A6})$$

and the real part is given as

$$\text{Re}[w_i(\omega^2)] = \begin{cases} \left[\frac{E_{23} \ln \left| \frac{X_2}{X_3} \right| (E_{13} - E_{21})}{\omega_1^2 - \omega_3^2} + \frac{\omega_2^2 - \omega_3^2}{2(\omega_1^2 - \omega_3^2)^2} \right] S_t, & i = 1, \\ \left[\frac{E_{23} \ln \left| \frac{X_2}{X_3} \right| E_{23} - E_{31}}{\omega_1^2 - \omega_3^2} + \frac{1}{2(\omega_1^2 - \omega_3^2)} \right] S_t, & i = 2, \\ \left[\frac{E_{23} \ln \left| \frac{X_2}{X_3} \right| (E_{31} + E_{32}) + \frac{1}{2}(E_{32} - E_{23}) + E_{31}}{\omega_1^2 - \omega_3^2} + \frac{\omega_3^2 - \omega_2^2}{2(\omega_1^2 - \omega_3^2)^2} \right] S_t, & i = 3. \end{cases} \quad (\text{A7})$$

Generally, $\text{Re}[w_i(\omega^2)]$ is the summation of Eqs. (A5) and (A7). However, in the case of energy degeneration at the vertices of a triangle [38] $\text{Re}[w_i(\omega^2)]$ is given by Eq. (A7) if $\omega_1^2 = \omega_2^2 \neq \omega_3^2$ and by Eq. (A5) if $\omega_1^2 \neq \omega_2^2 = \omega_3^2$.

To validate the implemented Green's function we compare the results obtained by summing over all planes with the results obtained with linear interpolation of the tetrahedron's elements [39]. Figure 7 shows the real and imaginary parts of the trace of the Green's function obtained by summing the contributions from all planes. The curves agree well with the results computed using the 3D tetrahedron method. We have, furthermore, compared the imaginary part of the Green's function to the phonon

density of states [$\rho(\omega)$]. Taking the $\rho(\omega)$ from PHONOPY [27] with the same IFCs and using the conversion $\rho(\omega) = 2\omega\rho(\omega^2)$, we obtain excellent agreement, Fig. 7.

-
- [1] D. G. Cahill, P. V. Braun, G. Chen, D. R. Clarke, S. Fan, K. E. Goodson, P. Kebblinski, W. P. King, G. D. Mahan, A. Majumdar *et al.*, *Appl. Phys. Rev.* **1**, 011305 (2014).
 - [2] W. Ng, M. Lourenco, R. Gwilliam, S. Ledain, G. Shao, and K. Homewood, *Nature (London)* **410**, 192 (2001).
 - [3] S. Nakamura, *Rev. Mod. Phys.* **87**, 1139 (2015).
 - [4] S. I. Kim, K. H. Lee, H. A. Mun, H. S. Kim, S. W. Hwang, J. W. Roh, D. J. Yang, W. H. Shin, X. S. Li, Y. H. Lee *et al.*, *Science* **348**, 109 (2015).
 - [5] P. Klemens, *Proc. Phys. Soc., London, Sect. A* **68**, 1113 (1955).
 - [6] P. Carruthers, *Rev. Mod. Phys.* **33**, 92 (1961).
 - [7] K. Ohashi, *J. Phys. Soc. Jpn.* **24**, 437 (1968).
 - [8] B. Deng, A. Chernatynskiy, P. Shukla, S. Sinnott, and S. Phillipot, *J. Nucl. Mater.* **434**, 203 (2013).
 - [9] Y. Ni, S. Xiong, S. Volz, and T. Dumitric, *Phys. Rev. Lett.* **113**, 124301 (2014).
 - [10] A. Katre and G. K. H. Madsen, *Phys. Rev. B* **93**, 155203 (2016).
 - [11] D. A. Broido, M. Malorny, G. Birner, N. Mingo, and D. A. Stewart, *Appl. Phys. Lett.* **91**, 231922 (2007).
 - [12] K. Esfarjani, G. Chen, and H. T. Stokes, *Phys. Rev. B* **84**, 085204 (2011).
 - [13] T. Yamamoto and K. Watanabe, *Phys. Rev. Lett.* **96**, 255503 (2006).
 - [14] N. Mingo, *Phys. Rev. B* **74**, 125402 (2006).
 - [15] J.-S. Wang, J. Wang, and N. Zeng, *Phys. Rev. B* **74**, 033408 (2006).
 - [16] P. Chen, N. A. Katcho, J. P. Feser, W. Li, M. Glaser, O. G. Schmidt, D. G. Cahill, N. Mingo, and A. Rastelli, *Phys. Rev. Lett.* **111**, 115901 (2013).
 - [17] N. A. Katcho, J. Carrete, W. Li, and N. Mingo, *Phys. Rev. B* **90**, 094117 (2014).
 - [18] A. Katre, J. Carrete, and N. Mingo, *J. Mater. Chem. A* **4**, 15940 (2016).
 - [19] J. R. K. Bigger, D. A. McInnes, A. P. Sutton, M. C. Payne, I. Stich, R. D. King-Smith, D. M. Bird, and L. J. Clarke, *Phys. Rev. Lett.* **69**, 2224 (1992).
 - [20] F. Liu, M. Mostoller, V. Milman, M. F. Chisholm, and T. Kaplan, *Phys. Rev. B* **51**, 17192 (1995).
 - [21] J. Hirth and J. Lothe, *Theory of Dislocations* (Krieger, Malabar, FL, 1982).
 - [22] See Supplemental Material at <http://link.aps.org/supplemental/10.1103/PhysRevB.95.245304> for convergence tests and details of the calculation of the IFCs.
 - [23] N. Mingo, K. Esfarjani, D. A. Broido, and D. A. Stewart, *Phys. Rev. B* **81**, 045408 (2010).
 - [24] A. Kundu, N. Mingo, D. A. Broido, and D. A. Stewart, *Phys. Rev. B* **84**, 125426 (2011).
 - [25] G. Kresse and J. Furthmüller, *Phys. Rev. B* **54**, 11169 (1996).
 - [26] G. Kresse and D. Joubert, *Phys. Rev. B* **59**, 1758 (1999).
 - [27] A. Togo, L. Chaput, and I. Tanaka, *Phys. Rev. B* **91**, 094306 (2015).
 - [28] W. Li, J. Carrete, N. A. Katcho, and N. Mingo, *Comput. Phys. Commun.* **185**, 1747 (2014).
 - [29] S.-i. Tamura, *Phys. Rev. B* **27**, 858 (1983).
 - [30] G. Gottstein, *Physical Foundations of Materials Science* (Springer, Berlin/Heidelberg, 2004).
 - [31] Z. Wang, J. E. Alaniz, W. Jang, J. E. Garay, and C. Dames, *Nano Lett.* **11**, 2206 (2011).
 - [32] G. Chen and M. Neagu, *Appl. Phys. Lett.* **71**, 2761 (1997).
 - [33] H.-S. Kim, S. D. Kang, Y. Tang, R. Hanus, and G. J. Snyder, *Mater. Horiz.* **3**, 234 (2016).
 - [34] X. Yang, J. Carrete, and Z. Wang, *Appl. Phys. Lett.* **108**, 113901 (2016).
 - [35] V. V. Bulatov, L. L. Hsiung, M. Tang, A. Arsenlis, M. C. Bartelt, W. Cai, J. N. Florando, M. Hiratani, M. Rhee, G. Hommes *et al.*, *Nature (London)* **440**, 1174 (2006).
 - [36] D. Kotchetkov, J. Zou, A. Balandin, D. Florescu, and F. Pollak, *Appl. Phys. Lett.* **79**, 4316 (2001).
 - [37] S. Kurganskii, O. Dubrovskii, and E. Domashevskaya, *Physica Status Solidi B* **129**, 293 (1985).
 - [38] J. A. Ashraff and P. D. Loly, *J. Phys. C* **20**, 4823 (1987).
 - [39] P. Lambin and J. P. Vigneron, *Phys. Rev. B* **29**, 3430 (1984).
 - [40] J. Carrete, B. Vermeersch, A. Katre, A. van Roekeghem, T. Wang, G. K. H. Madsen, and N. Mingo, [arXiv:1704.04142](https://arxiv.org/abs/1704.04142).